Simulation of the Performance of ESA's Herschel/SPIRE Imaging Fourier Transform Spectrometer

John V. Lindner*[a], David A. Naylor[a], Bruce M. Swinyard[b],
[a]Department of Physics, University of Lethbridge, Lethbridge, Alberta, Canada.
[b]Rutherford Appleton Laboratory, Chilton, Oxfordshire, England.

ABSTRACT

The Spectral and Photometric Imaging Receiver (SPIRE) is one of three scientific instruments on ESA's Herschel mission. The spectroscopic capabilities of SPIRE are provided by an imaging Fourier transform spectrometer (IFTS). A software simulator of the IFTS has been constructed to predict the instrument performance under operational conditions. We describe in detail the design and integration of the simulator. Examples of simulated data of astronomical targets are presented.

Keywords: Herschel, SPIRE, Imaging Fourier Transform Spectrometer, Software Simulation

1. INTRODUCTION

Though still in its infancy, infrared space astronomy has, in the past 20 years, provided the astronomical community with a wealth of observational data. The joint US-Dutch-British Infrared Astronomical Satellite (IRAS), launched in 1983, was the first to indicate that galaxies emit a large portion of their luminosity in the infrared and submillimeter spectral regions.[1] This is largely due to the absorption and re-emission of uv radiation by dust and cold gas. Observations over the last decade with ESA's Infrared Space Observatory[2] and the Submillimeter Common-User Bolometer Array[3] camera on the James Clerk Maxwell Telescope further reinforced these ideas. High-redshift galaxies present another class of interesting objects, whose peak emission is doppler shifted into the infrared, thereby making observable to infrared telescopes what otherwise would have been obscured by intervening gas and dust.

ESA's Herschel Space Telescope[4] is the next technological advance in far infrared astronomy. With a 3.5 m passively cooled primary mirror, cryogenically cooled instrument payload, and no atmospheric contributions, Herschel will have an unparallelled sensitivity at far infrared and submillimeter wavelengths. One of Herschel's three instruments, the Spectral and Photometric Imaging REceiver[5] (SPIRE), will contain a 3-band photometer and an imaging Fourier transform spectrometer (IFTS). The IFTS will fulfill two of Herschel's primary scientific aims: follow-up spectroscopic measurements for galactic and extragalactic surveys. In contrast to standard Fourier transform spectroscopy where the interferogram is sampled in equal increments of optical retardation, the SPIRE IFTS will function in a time-sampled mode, which requires sophisticated Fourier analysis techniques.

To highlight preferred operational modes prior to launch, a Monte Carlo simulation of the IFTS has been developed in IDL,[6] expanding on an earlier version written by Bruce Swinyard.[7] A realistic simulation is achieved by including all significant noise sources from the mechanical, optical, and electrical subsystems, utilising experimental data provided by the teams supplying these subsystems. The simulator will provide realistic FTS data to the SPIRE Instrument Control Center's (ICC) Data Processing and Science Analysis Software development teams so they can effectively test their workpackages. This simulator complements Bruce Sibthorpe's work on a simulation of the SPIRE photometer.[8]

This paper will describe the current state of the simulator, its role as a diagnostic and predictive tool, and discuss future plans for its development and usage. Section 2 briefly describes the physical design of the SPIRE IFTS. The architectural design and operation of the simulation is outlined in detail in Sec. 3. Section 4 lists current results.

*E-mail: john.lindner@uleth.ca; Telephone: (403) 329-2719; Fax: (403) 329-2057; www.uleth.ca/phy/naylor/

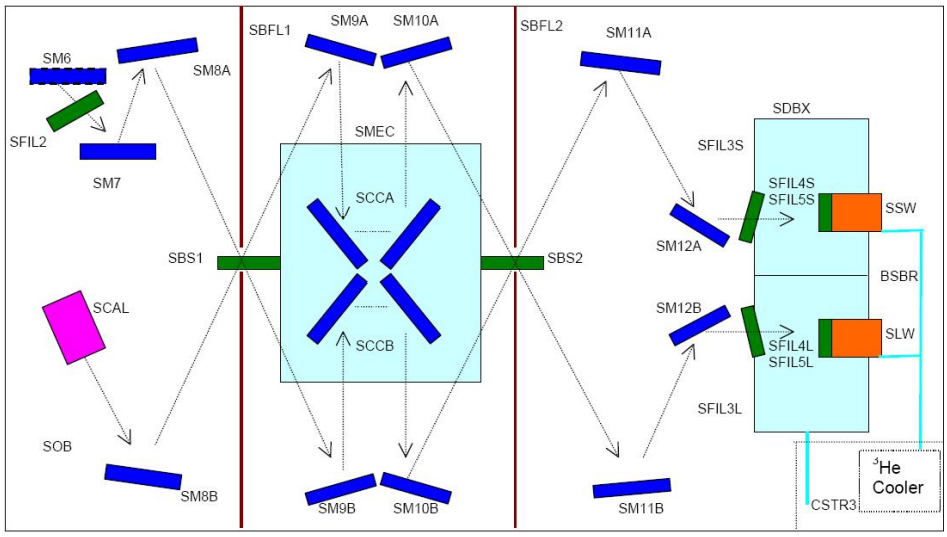

Figure 1. Schematic Design of Mach-Zehnder design used in SPIRE Imaging FTS.[10] Arrows indicate propagation of light; which enter at SM6, the pick-off mirror.

2. INSTRUMENT OVERVIEW

The SPIRE IFTS (Fig. 1) is based on a modified Mach-Zehnder design[9] utilising intensity beam-splitters (SBS1 and SBS2). This design ensures that, unlike a traditional Michelson Interferometer, both input and output ports are accessible. There are two input pupils, one corresponding to the image of the primary mirror (SFIL2) and the other corresponding to the spectrometer calibrator SCAL (SM8B), which is used to null the background telescope radiation.

Optical retardation is achieved with the Spectrometer Mechanism (SMEC), a moving back-to-back rooftop mirror. The SMEC position readout uses a Heidenhain encoder. SMEC has a linear travel from -3.2 mm to 32 mm (referenced to zero optical path difference), which provides a maximum resolution of 0.047 cm^{-1} (1418 MHz).[5] In this design, a change in stage position of Δx corresponds to a change in the optical path of $4\Delta x$.[9] SMEC can be operated in either rapid scan or step-and-integrate mode.

Two detector arrays are placed at the two output ports of the interferometer.[5] There are 37 detectors in the short wavelength array, SSW, which covers the range from 200 to 325 μm. There are 19 detectors in the long wavelength array, SLW, which covers the range from 315 to 670 μm. Both detectors arrays are arranged in hexagonal patterns. Radiation is detected with feedhorn-coupled spider-web bolometers, using neutron-transmutation doped germanium thermometers. The bolometers have a thermal time constant and their response to changes in the incident radiation is equivalent to a low-pass filter. Subsequently, the bolometer signal is filtered, amplified and digitized.

3. SIMULATOR DESIGN

The goal of the Spire imaging FTS Simulator (SIFTSS) is to generate a synthetic interferogram, including realistic estimates of all noise sources, from an input spectrum. In the basic operation of the simulator, users can draw from a standard set of synthetic astronomical hypercubes having 2 spatial and 1 spectral dimension. Alternatively, users can create their own hypercube. The simulator models all components of the IFTS and returns an interferogram for each pixel.

SIFTSS is primarily concerned with random errors, not systematic ones. For example, photon noise has been included, whereas the effects of a misaligned mirror has not. The following components of SPIRE have been

included in the model: detectors and detector electronics (including electrical post-filtering), filters, moving mirror scanning mechanism, beamsplitters, optics, and the calibration source. Each component, with its associated noise contributions, has been modelled separately.

Currently, users interface with SIFTSS via the IDL command line. It is anticipated that the final version of SIFTSS will include a graphical user interface. The primary parameters specified by the user are the number and length of scans, and the spectrometer observatory function (SOF), which defines the operating mode of the stage and the sky mapping strategy. SOF1 (point source mapping) and SOF2 (jiggle mapping) are both rapid scan modes where the user defines the stage speed and the SCAL temperature. SOF3 (point source mapping) and SOF4 (jiggle mapping) are both step-and-integrate modes where the user defines the chop frequency (the calibration source is not used in Step-and-Integrate mode since it would lower the signal-to-noise ratio). The discussion in this paper will be limited to SOF1, point source rapid scan, as the current version of the simulator only operates in this mode.

3.1. Master time

Central to the concept of SIFTSS is the master clock. A master time array is defined by the requested scan length and velocity, conveniently sampled at 3.125 kHz, one hundredth of the SPIRE digital processing unit (DPU) clock speed.[10] The master time is used to define both the ideal SMEC position and the bolometer signal as a function of time. Like the DPU clock, the master time is assumed to be without error and provides a reference point for all measurements. For the remainder of the paper, all references to time imply the master time grid.

3.2. Simulated spectra

The user can supply a hypercube, having 2 spatial and 1 spectral dimension, or use one of a basic set of predefined hypercubes (e.g.. point or extended sources of continuum emission with/without emission/absorption lines).

The synthetic spectra, in units of $\mathrm{Wm^{-2}str^{-1}(cm^{-1})^{-1}}$, are converted to $\mathrm{W(cm^{-1})^{-1}}$ using the area, A, of the Herschel primary mirror and solid angle, Ω, of the detector's field of view projected onto the sky. Added to the astronomical spectra is the telescope emission, which is modelled as a blackbody at 80 K with an emissivity of 4%. Assuming a conserved throughput, the blackbody spectrum of the telescope emission is converted to $\mathrm{W(cm^{-1})^{-1}}$ using the Lagrange Invariant,

$$A\Omega = \lambda^2, \tag{1}$$

where $A\Omega$ is in units of $\mathrm{m^2str}$. The spectrum of the calibration source (SCAL) is also considered to be a blackbody at 80 K with an emissivity of 4% and is computed in the same manner as the telescope background. However, provision is made within SIFTSS for both the Herschel primary mirror and SCAL's emissivity and temperature to be varied.

SIFTSS also accounts for two important optical effects. First, since light that reaches off-axis pixels traverses the interferometer at an angle α with respect to the optical axis, the effective sampling of off-axis interferograms occurs on a position sampling grid shortened by a factor of $\cos\alpha$. Second, SIFTSS accounts for the natural apodization of the interferogram due to the finite aperture of SPIRE. This is accomplished by multiplying the interferogram by $\mathrm{sinc}(\frac{\sigma x \Omega_{pix}}{2\pi})$, where Ω_{pix} is the solid angle of a single pixel.[11]

In order to study time-varying effects such as the drift of the telescope temperature and pointing jitter, it is necessary to add a fourth dimension to the hypercube, corresponding to the master time array (i.e. each time sample corresponds to a slightly different hypercube).

3.3. Beamsplitters

The radiation from the astronomical source, including the telescope emission, is combined with that from the blackbody source (SCAL) at the first beamsplitter (SBS1). Provision has been made to include the reflection and transmission properties of the beamsplitter when those data becomes available. For now, the reflection and transmission efficiencies are assumed to be exactly 50%. SIFTSS also accounts for the approximately π radians phase shift of the reflected beam. Additionally, a small wavelength-dependent phase shift has been observed in the transmitted beam.[12] This effect is subject to ongoing investigation and will be included in a later version of SIFTSS.

3.4. SMEC

For each of the two output beams of the first beamsplitter (SBS1), the phase shift (radians), ϕ, in each arm of the interferometer due to a linear translation x from the zero path difference (zpd) location of SMEC is given by

$$\phi = e^{\pm i 2\pi\sigma(2x\cos\alpha)}, \tag{2}$$

where σ is the wavenumber. The plus-minus sign in Eqn. 2 reflects the fact that the phase leads for one arm of the interferometer and lags for the other.

The SMEC velocity jitter is expected to be the largest noise source in the SPIRE IFTS. The velocity of the SMEC stage is not constant, thus equal increments in time do not correspond to equal increments in position. There are three primary components to the velocity noise: servo-loop tracking, and random and resonance effects. Data from tests conducted at Goddard Space Flight Center (GSFC), with the second SMEC prototype, indicated that the velocity varies in a sinusoidal fashion about the set value of 0.5 mm s^{-1}.[7] This can be traced directly to the servo-loop controlling the velocity. To simulate this variation in SIFTSS, the position-time data from GSFC was used to produce a position error grid, defined as the difference between the measured position and the theoretical position (assuming a constant velocity). From that position error, a power spectrum (effectively a probability distribution function) was determined, and is shown in Fig. 2 (solid line). Note the peak at approximately 50Hz; this is the frequency at which the servo-loop operates. A random number generator (with a mean of zero and a standard deviation of one) is used to extract randomized position errors from the fit to the calculated power spectrum of Fig. 2, shown as a dotted-dashed line. Although it is not visible in Fig. 2, the peak at 50 Hz is included in the simulation. These simulated position errors are then added to the ideal SMEC position values outlined in Sec. 3.1.

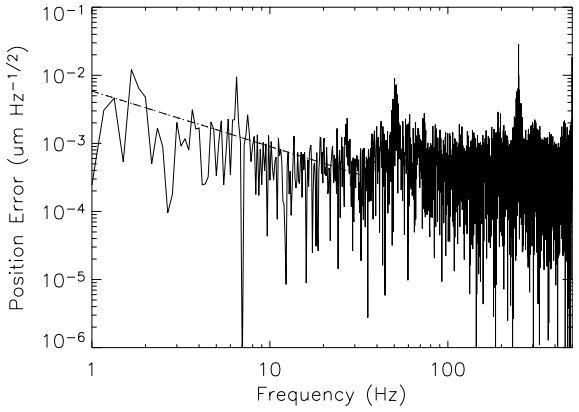

Figure 2. Power Spectrum of position error for SMEC Prototype 2, showing original GSFC data (solid line) and the fit to GSFC data (dotted-dashed line).

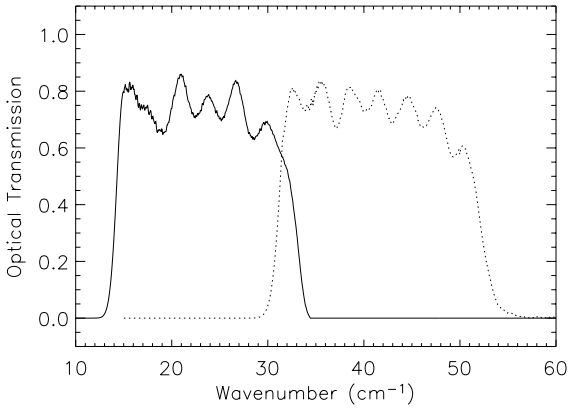

Figure 3. Profile of Spectrometer long wavelength (solid line) and short wavelength (dotted line) detector arrays optical transmission

Additionally, it is not necessary to specifically include position error from the Heidenhain encoder since it is already included in the SMEC position-time data used to create the power spectrum. It is not easily possible to separate the two noise sources.

3.5. Bolometers and post-detection

The two outputs of the second beamsplitter (SBS2) are directed to one of the two complementary detector arrays (SSW or SLW), as described in Sec. 2. The optical transmission of the 2 detector subsystems, accounting for the filters and the waveguide cutoff, is shown in Fig. 3.

For each time sample, corresponding to an optical retardation z=4x, the intensity (W), $I(z)$, is calculated by integrating over the bandwidth from σ_{Lo} to σ_{Hi},

$$I(z) = \int_{-\infty}^{\infty} B(\sigma) e^{-2\pi i \sigma z} d\sigma = \sum_{\sigma_{Lo}}^{\sigma_{Hi}} B(\sigma) e^{-2\pi i \sigma z} \Delta\sigma. \tag{3}$$

The interferogram hypercube now consists of 2 spatial dimensions and one dimension of time, corresponding to optical retardation.

Bolometers operate on the principle that absorbed radiation changes the resistance of the bolometer. In the case of SPIRE, the spider-web bolometers are cooled by a heat sink held at 300 mK.[13] Incoming radiation is absorbed by the spider-web, and the heat is conducted to the crystal thermometer, thereby changing its resistance. Under a constant bias current, that change in resistance leads to a change in voltage, which can be measured. The thermal properties of the bolometer are well modelled as an electrical RC low-pass filter circuit,[14] where the responsivity (W V^{-1}), dV/dQ, is equal to

$$\frac{dV}{dQ} \propto (1 + \omega^2 \tau^2)^2, \tag{4}$$

given the angular frequency (radians s^{-1}), ω, and the thermal time constant (s), τ, defined by

$$\tau = \frac{C}{G}, \tag{5}$$

where C is the heat capacity (J K^{-1}) of the bolometer and G is the thermal conductance (W K^{-1}) of the link between the bolometer and the heat sink.[14] For SSW and SLW, the time constants are 8 and 14 ms, respectively.[10] Given the measured responsivity of 10^8 V W^{-1}, the detected power, $I(z)$, can be converted to a voltage. Photon noise, equal to the square root of the number of detected photons, and detector noise of 15 nV $Hz^{-1/2}$ are added in quadrature to the interferogram.

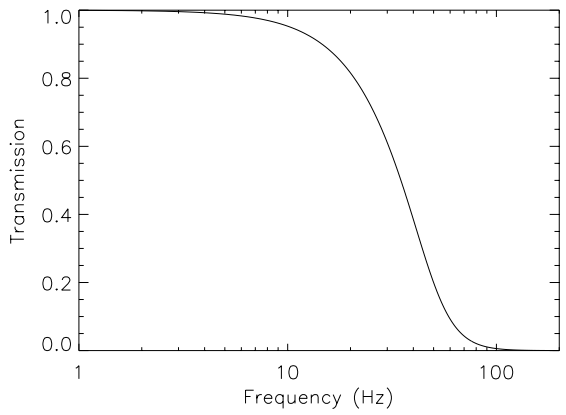

Figure 4. Transmission profile of electrical filter

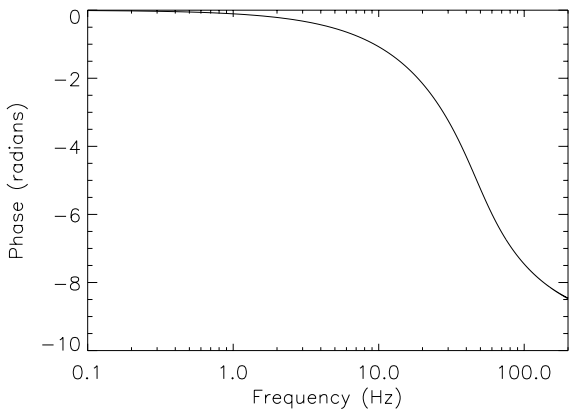

Figure 5. Phase profile of the electrical filter

The mean value of the interferogram is subtracted from each point in the interferogram to simulate the high-pass filter that removes the DC offset. The model also includes a pre-amplifier gain of 1000.[10] The final electrical filter is a 6-pole Bessel function, those transmission and phase profiles are shown in Figs. 4 and 5, respectively. To apply the filter, the interferogram is Fourier transformed to the frequency domain, where it is multiplied by the complex electrical filter profile. The spectrum is then inverse Fourier transformed back to the interferogram domain.

3.6. Simulator output

The over-sampled interferogram is re-sampled down to the SPIRE signal sampling frequency of 80 Hz.[10] The interferogram signal is digitized with a 5 volt full-scale 16-bit ADC. The SMEC position is also interpolated onto a time grid that corresponds to the 250 Hz readout from SPIRE.[7] The position is converted to an optical path difference (opd) using the factor of 4 for the Mach-Zehnder design.[9]

4. RESULTS AND DISCUSSION

Three groups of tests were conducted to evaluate the performance of SIFTSS. First, tests were performed on the individual modules with no noise (Sec. 4.1). Tests were then conducted on the whole simulator, with all noise sources included (Sec. 4.2). Section 4.3 describes simulation of a whole pixel map of the sky.

4.1. Module tests

There are two primary routines that modify the spectra (discussed below), one for the interferometer and one for the detection subsystem. Individual tests were conducted to confirm that both these modules performed as predicted by theory as outlined in Sec. 3. For these tests, no noise sources were included. The input spectrum consisted of a blackbody at a temperature of 15 K, with an emissivity index β of 1.5. The spectrum spanned the range from 15 to 55 cm^{-1} with a resolution of 0.16 cm^{-1}, and contained a single emission line of intensity 9.6×10^{-8} $\mathrm{Wm}^{-2}\mathrm{str}^{-1}(\mathrm{cm}^{-1})^{-1}$ at 38.4 cm^{-1}. A stage speed of 1.0 mm s^{-1} and a double-sided stage scan length of 3.2 mm were employed for the module tests, giving an unapodized resolution of $\sim$0.47 cm^{-1}. Ω was taken to be the full-width half-maximum (FWHM) of an SSW pixel, which corresponds to $\sim 6.0 \times 10^{-9}$ str.

4.1.1. Interferometer

The first module that the spectral hypercube encounters is the interferometer. This module accounts for the effects of the first beamsplitter (SBS1), phase shifts due to SMEC, and the second beamsplitter (SBS2). Figure 6 shows the two inputs to the beamsplitter module, represented as electric fields. Figure 7 shows the output ports of the first beamsplitter module, denoted E_1 and E_2 (V m^{-1}). As expected, the telescope background is cancelled out entirely by the calibration source.

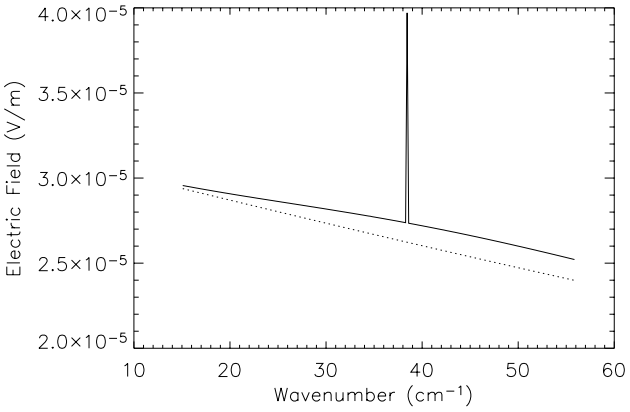

Figure 6. Input to first beamsplitter, showing both the signal from sky and telescope background (solid line) and the signal from the SCAL (dotted line).

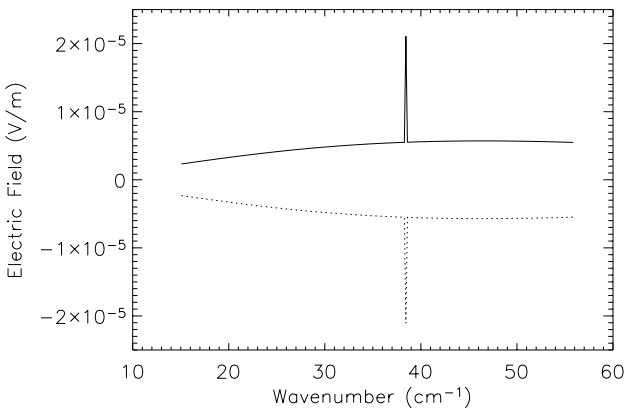

Figure 7. Electric field exiting first beamsplitter, showing the down beam (solid line) and the up beam (dotted line).

The frequency-dependent phase difference between the two beams traversing the arms of the interferometer is given by Eqn. 2. Interference arises when the two beams are recombined at the second beamsplitter (SBS2). Thus, the output ports of the second beamsplitter (V m^{-1}), E_3 and E_4, are given by

$$\begin{aligned} E_3 &= T_\sigma E_1 e^{i2\pi\sigma(2x\cos\alpha)} + R_\sigma E_2 e^{-i2\pi\sigma(2x\cos\alpha)}, \\ E_4 &= R_\sigma E_1 e^{i2\pi\sigma(2x\cos\alpha)} + T_\sigma E_2 e^{-i2\pi\sigma(2x\cos\alpha)}, \end{aligned} \quad (6)$$

where T_σ and R_σ are the transmission and reflection profiles of the second beamsplitter as a function of wavenumber. The electric field, E, is then converted to a power (W) using the Poynting vector,

$$I(z) = A\frac{c\varepsilon_o}{2}E^2, \tag{7}$$

where ε_o is the permittivity of free space, and c is the speed of light.

4.1.2. Detection subsystem

Fig. 8 shows the ideal bolometer-sampled interferogram (solid line) near zpd for the SSW detector array after calculating Eqns. 6 and 7 at each opd. As there are no noise sources present, equal increments in time correspond to equal increments in SMEC position, resulting in a symmetric interferogram. Overplotted as a dotted line is the same interferogram, to which the detector bolometer response has been applied. As mentioned in Sec. 3.5, the bolometer acts like a low-pass filter, attenuating high-frequency components. The position of zpd is also shifted by the bolometer response, introducing an asymmetry in the interferogram.

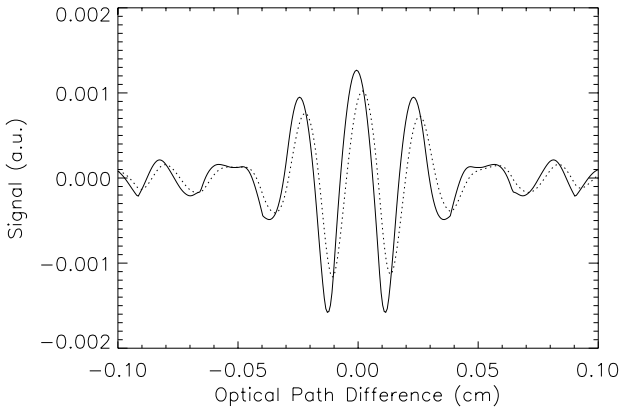

Figure 8. Ideal bolometer-sampled interferogram (solid line) and real bolometer-sampled interferogram (dotted line), near zpd. (a.u. is arbitrary units)

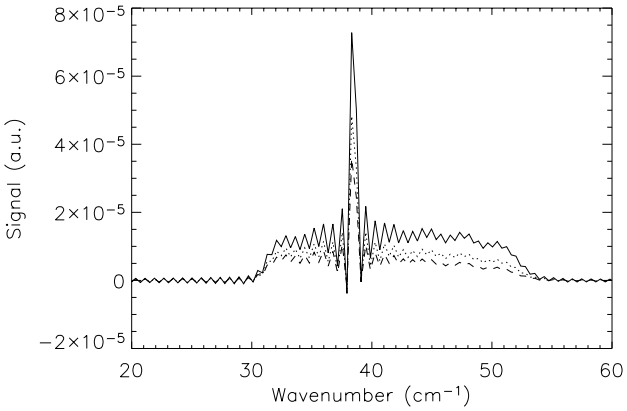

Figure 9. Real component of spectra from SIFTSS-generated interferograms, showing ideal bolometer-sampled spectrum (solid line), real bolometer-sampled spectrum (dotted line), and electrical filtered spectrum (dashed line).

The next figure (Fig. 9) shows the spectrum corresponding to the ideal bolometer-sampled interferogram (solid line). As can be seen, the real bolometer-sampled spectra (dashed line) has a distinct roll-off at high frequencies due to the low-pass nature of the RC circuit. A further roll-off is noted with the application of the electrical filter (dashed line). The signal is only detected in the region of optical transmission allowed by the SSW detector subsystem (Fig. 3). The ringing is seen because the width of the emission line is smaller than the resolution of the scan. Even with these effects, the line center was measured at 38.3 cm^{-1}, consistent with the theoretical value of 38.4 cm^{-1}within the resolution of the scan.

4.2. Noise tests

The second group of tests studied the effect of varying velocity error. To simplify this analysis, it was assumed that the detector bandpass subsystems have unity transmission efficiency.

The input blackbody spectrum from Sec. 4.1 was common to all the tests outlined here. A stage speed of 0.5 mm s^{-1} and double-sided stage scan length of 3.2 mm were employed. With velocity noise included, the fast-Fourier transform (FFT) can no longer be employed to compute wavenumber-gridded spectra from SIFTSS-generated interferograms since z is no longer regularly-gridded; that would require the use of the more complex irregularly-gridded Fourier transform. As such, a frequency grid is employed, calculated from the regularly-spaced master time grid. Photon noise and electrical noise were included at the levels described in Sec. 3.4.

The velocity jitter of the SMEC moving mirror is determined using a fit to a probability distribution function, as discussed in Sec. 3.4. As a check of the technique outlined in Sec. 3.4, the position error was calculated from position-time data generated by SIFTSS. From that, we determined a probability distribution of the synthetic position error, shown as a solid line in Fig. 10. Overplotted as a dotted-dashed line is the original fit used to simulate the error. The simulated power spectrum agrees well with the original data from the second SMEC prototype, shown in Fig. 2. Note that the 50 Hz servo-tracking peak is visible in Fig. 10. The velocity jitter in Fig. 10 corresponds to a velocity error of 15%.

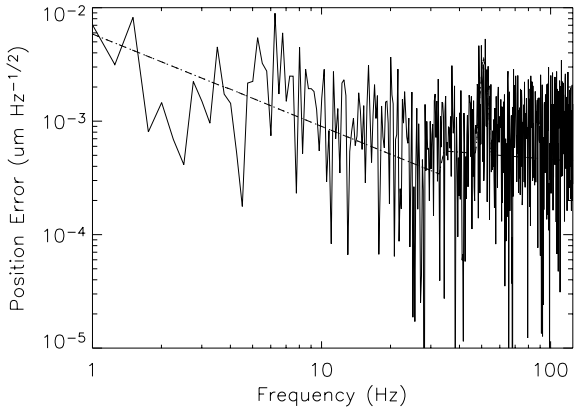

Figure 10. Power Spectrum of synthetic SMEC position error, showing SIFTSS-generated position error (solid line) and the fit to the GSFC position-time data (dotted-dashed line).

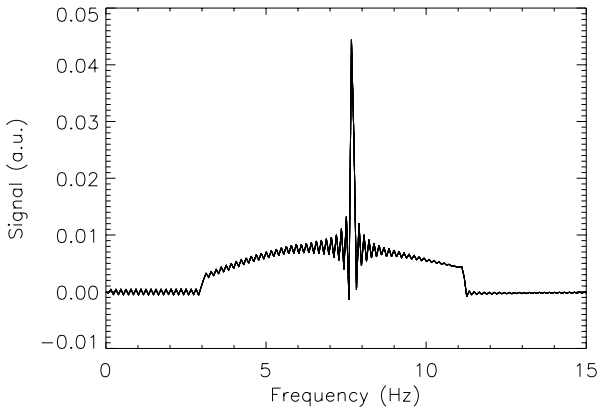

Figure 11. Ten spectra, from SIFTSS-generated interferograms.

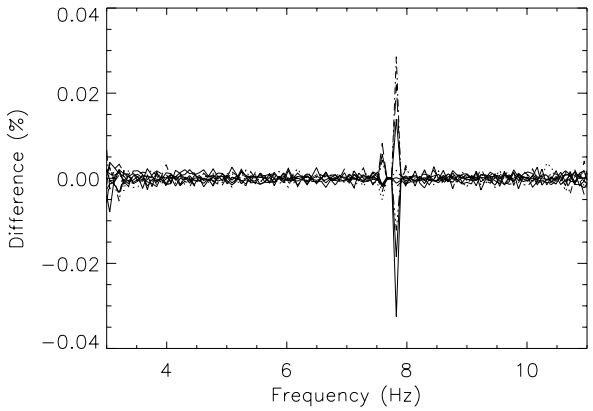

Figure 12. Percentage error between each of the ten spectra and the group-average spectrum.

In order to show that results from SIFTSS were reproducible, the simulator was executed 10 times with a stage speed of 0.5 mm s^{-1} and a double-sided stage scan length of 3.2 mm. Figure 11 shows the spectra from these ten runs, which all show excellent agreement. Fig. 12 shows the percent difference between each individual spectrum and the group-average spectrum. The large error near 8 Hz corresponds to the emission line at 38.4 cm^{-1}. As can be seen, the largest error is no more than 0.03% percent for all frequencies.

4.3. Simulated astronomical model

Up to this point, only single pixels were considered when the simulator was executed. However, the power of the SPIRE IFTS is in conducting detailed spectral maps of the sky. Thus, this section will describe the application of the simulator to a full SPIRE detector array. The input is a synthetic hypercube of an expanding gas cloud, with a hemisphere of CO emission lines, shown in Fig. 13.

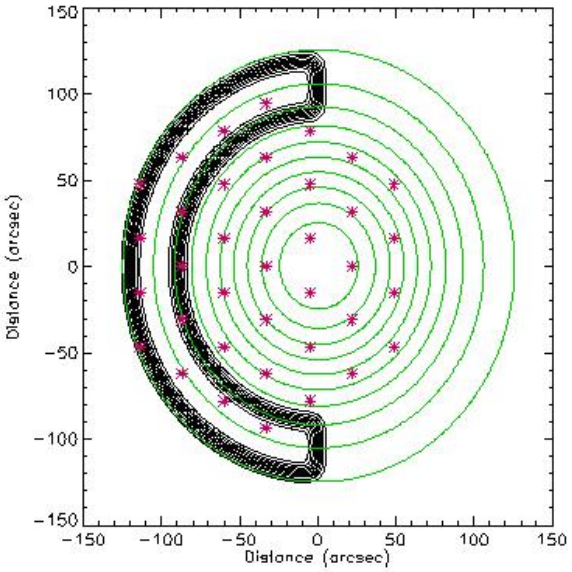

Figure 13. Contour map of simulated sky employed to test SIFTSS

Fig. 13 shows a contour map of the simulated sky emission with the locations of the SSW pixels (stars) superimposed. The circular contours represent a dense cold region of continuum emission peaking in density, and therefore flux, at the center of the map. The semi-circular contours represent the intensity of line emission from a warmer region on the surface of the cold dense cloud. Although artificial, this situation does arise in Bok globules or starless cores where the surface of the dense cloud is illuminated by interstellar uv emission or in star formation regions.[15] For simplicity, we have assumed only one emitting species, CO, with line strengths on the order of a few 10^{-14} W m^{-2} and included all transitions that fall within the SPIRE band. The peak of the continuum emission represents $\sim$1 Jy in the SPIRE SSW beam.

Figure 14 shows the input hypercube to the full scan. There are 37 spectra, each corresponding to one of SSW's 37 pixels. Thirteen pixels in the map were situated on the CO emission line hemisphere. The gas cloud has a blackbody temperature of 15 K with $\beta = 1.5$. Each spectrum is sampled from 15 to 55 cm^{-1} with a resolution of 0.16 cm^{-1}. Each pixel covers a solid angle of $\sim 6.0 \times 10^{-9}$ str on the sky and their centers are separated by $\sim$0.5 arc-minutes.

As before, SIFTSS was executed with a velocity of 0.5 mm s^{-1} and a double-sided stage scan length of 3.2 mm. All noise sources (photon, velocity Jitter, electrical) are included at the nominal levels stated above. As in Sec. 4.2, the detector subsystems have unity transmission efficiency. Figure 15 shows the hypercube calculated from the raw (i.e. not phase-corrected) zero-padded interferograms generated by SIFTSS. Though this test scan was performed at the SPIRE IFTS' lowest theoretical resolution, line centers were easily determined in spectra where lines were present. Table 1 shows the average line centers for each line of the 13 spectra. The measured line centers are consistent with the theoretical line centers within the error bars of the measured lines.

Figure 16 shows the input spectrum (dotted line) and the SIFTSS-generated spectrum (solid line) of spectrum 23 from Fig. 14. The attenuation of high-frequency spectral components due to the bolometer time constant is

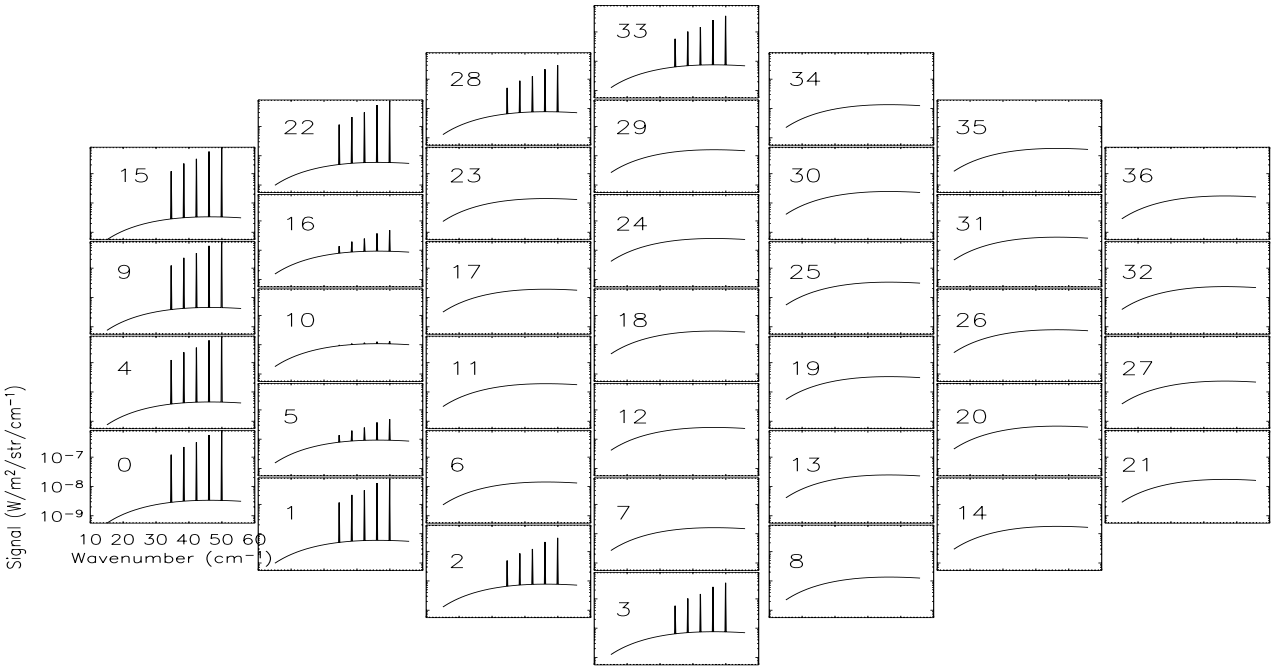

Figure 14. Input spectral hypercube of synthetic sky. For clarity, the scales are only shown for spectrum 0, and are identical for each spectra.

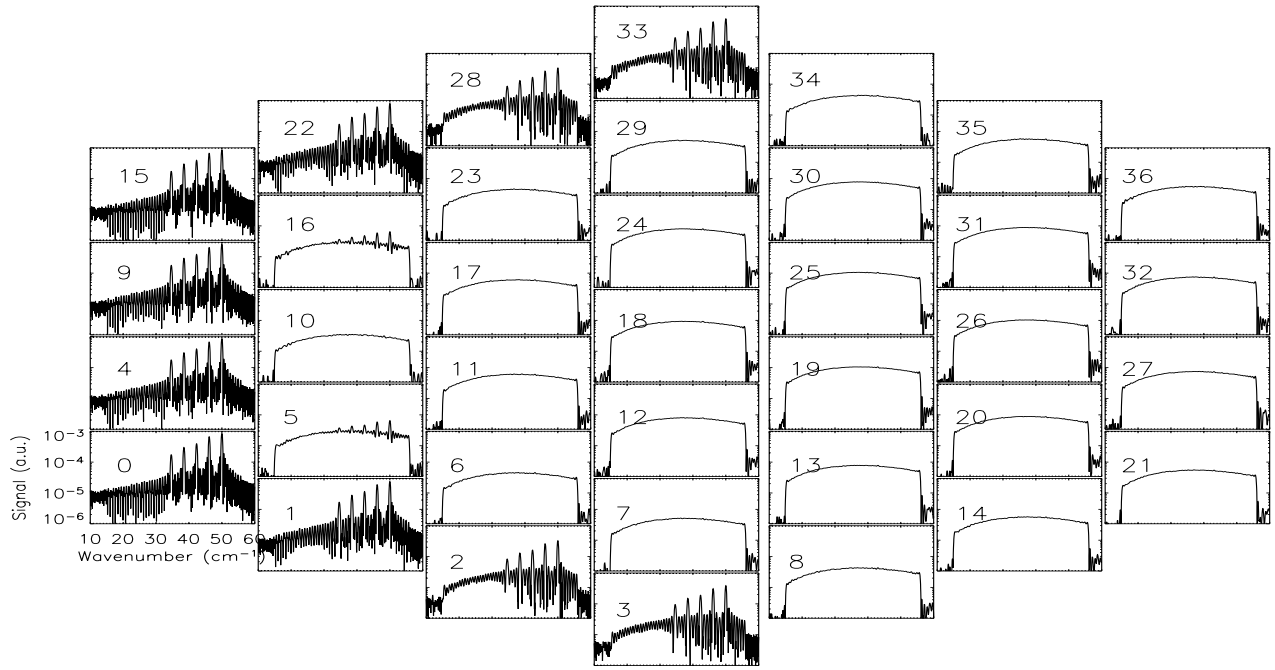

Figure 15. SIFTSS output of spectral hypercube of synthetic sky. For clarity, the scales are only shown for spectrum 0, and are identical for each spectra.

	Line Center (cm^{-1})	
	Theory	Measured
Line 1	34.60	34.62 ± 0.47
Line 2	38.44	38.47 ± 0.47
Line 3	42.28	42.31 ± 0.47
Line 4	46.10	46.14 ± 0.47
Line 5	49.94	50.02 ± 0.47

Table 1. Line Centers for each of the 5 lines averaged from spectra 0, 1, 2, 3, 4, 5, 9, 15, 16, 22, 28, and 33 from Fig. 14.

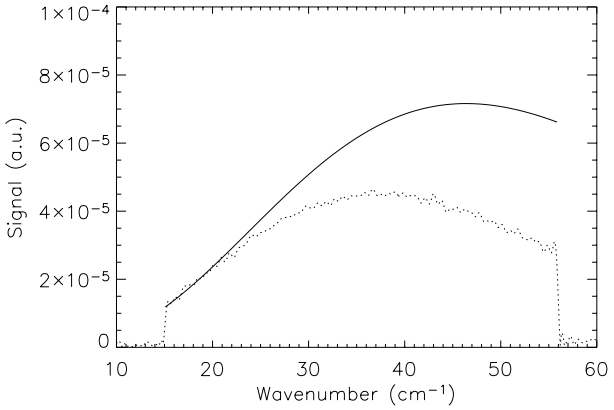

Figure 16. Spectrum 23, where the input spectrum (solid line) is scaled to the continuum of the SIFTSS-generated spectrum (dotted line) at $20 cm^{-1}$.

clearly evident, and shifts the peak of the curve to shorter wavenumbers. Therefore, it is no longer possible to apply Wien's Law to make an accurate determination of the blackbody temperature. In the case of Fig. 16, such a calculation returns a temperature of 10.8 ± 0.15 K, whereas the theoretical value was 15 K.

5. CONCLUSION

A Monte Carlo software simulator has been written in IDL to model the performance of the Herschel-SPIRE IFTS. Current results indicate that the simulator is performing well, and as expected. Figure 9 and 16 illustrate several of the effects that the ICC software will need to correct for: ringing and attenuation of high-frequency components of the spectrum. Therefore, simulations from SIFTSS will be vital for testing the software design teams' data processing algorithms. The ultimate goal of the simulator is to provide the SPIRE design team with a diagnostic tool and the astronomical community with a powerful predictive tool to display the importance of this complex instrument.

This simulator consists of modules, which correspond to individual subsystems within the IFTS. This modular design allows for the latest performance characteristics of individual subsystems to be integrated, bringing added realism. Future versions will include second-order factors, such as the time-varying effects of the IFTS, which will complement the work being done to build a simulator of the SPIRE photometer.[8] Furthermore, the final interface and output data format for SIFTSS will mirror identically those of the SPIRE instrument itself, when it is flown on Herschel.

ACKNOWLEDGMENTS

The authors wish to thank Professor G.R.Davis, now Director of the James Clerk Maxwell Telescope, for negotiating and securing approval for Canada's participation in the SPIRE project. This work would otherwise not

have been possible.

JVL would like to thank Bruce Sibthorpe for his help with the bolometer model, Doug Griffin for taking the time to explain the post-processing electronics, Peter Hargrave for providing the SCAL temperature data, Tanya Lim and Steve Guest for advice on data formats, and Peter Ade for the beamsplitter data. JVL would especially like to thank Locke Spencer and Samuel Ronayette for providing a positive working environment. BMS would like to acknowledge the work of the team at LAM, who are building the spectrometer mechanism. This research is funded in part by grants from CIPI (JVL), CSA (JVL, DAN) and NSERC (DAN). SPIRE instrument development in the UK is funded by PPARC. Finally, JVL would like to thank the Rutherford Appleton Laboratories for providing him with everything necessary for this project over the past 6 months.

REFERENCES

1. D. B. Sanders and I. F. Mirabel, "Luminous Infrared Galaxies," *Annual Review of Astronomy and Astrophysics* **34**, p. 749, 1996.
2. R. Genzel, *The Universe as seen by ISO*, ch. Galaxies as seen by ISO. ESA Publications Division, SP-427, 1999.
3. W. S. Holland, E. I. Robson, W. K. Gear, C. R. Cunningham, J. F. Lightfoot, T. Jenness, R. J. Ivison, J. A. Stevens, P. A. R. Ade, M. J. Griffin, W. D. Duncan, J. A. Murphy, and D. A. Naylor, "SCUBA: a common-user submillimetre camera operating on the James Clerk Maxwell Telescope," *MNRAS* **303**, pp. 659–672, Mar. 1999.
4. G. Pilbratt, "Herschel Mission: Status and Observing Opportunities," *SPIE Proceedings: Optical, Infrared, and Millimeter Space Telescopes (this volume)* **5487**, (Glasgow, June 21-25), 2004.
5. M. Griffin, B. Swinyard, and L. Vigroux, "The Herschel: SPIRE Instrument," *SPIE Proceedings: Optical, Infrared, and Millimeter Space Telescopes (this volume)* **5487**, (Glasgow, June 21-25), 2004.
6. "Interactive Data Language, Research Systems Inc." http://www.rsinc.com.
7. B. M. Swinyard, K. Dohlen, D. Ferand, J.-P. Baluteau, D. Pouliquen, P. Dargent, G. Michel, J. Martignac, P. Ade, P. Hargrave, M. Griffin, D. Jennins, and M. Caldwell, "The Imaging FTS for Herschel SPIRE," *SPIE Proceedings: IR Space Telescopes and Instruments* **4850**, pp. 698–709, 2003.
8. B. Sibthorpe, A. Woodcraft, and M. Griffin, "A software simulator for the Herschel-SPIRE imaging photometer," *SPIE Proceedings: Optical, Infrared, and Millimeter Space Telescopes (this volume)* **5487**, (Glasgow, June 21-25), 2004.
9. P. Ade, P. Hamilton, and D. Naylor, "An Absolute Dual Beam Emission Spectrometer," in *Fourier Transform Spectroscopy: New Methods and Applications*, pp. 90–92, Optical Society of America, 1999.
10. D. Griffin, M. Griffin, and B. Swinyard, "SPIRE Design Document," Tech. Rep. SPIRE-RAL-PRJ-000620, Rutherford Appleton Laboratory, 2002.
11. R. Bell, *Introductory Fourier Transform Spectroscopy*, Academic Press, New York.
12. D. Naylor, 2004. Private communication.
13. G. Chattopadhyay, J. Glenn, J. J. Bock, B. Rownd, M. Caldwell, and M. J. Griffin, "Feedhorn Coupled Bolometer Arrays for PSIRE: Design, Simulation, and Measurements," *IEEE Transactions on Microwave Theory and Techniques* **51**, pp. 2139–2146, 2003.
14. M. J. Griffin and W. S. Holland, "The influence of background power on the performance of an ideal bolometer," *International Journal of Infrared and Millimeter Waves* **9**(10), pp. 861–875, 1988.
15. B. Nisini, P. Saraceno, C. Ceccarelli, T. Giannini, E. Tommasi, L. Spinoglio, and G. White, "High-J CO Line Emission from Young Stellar Objects: From ISO to First," *Proceedings of ESA Symposium: 'The Far Infrared and Submillimeter Universe* **ESA SP-401**, (Grenoble, France), 1997.